The Astrophysical Journal Supplement Series, 193:19 (15pp), 2011 March doi:10.1088/0067-0049/193/1/19
© 2011. The American Astronomical Society. All rights reserved. Printed in the U.S.A.

CO($J = 1$–0) IMAGING OF M51 WITH CARMA AND THE NOBEYAMA 45 m TELESCOPE

Jin Koda[1,2], Tsuyoshi Sawada[3,4], Melvyn C. H. Wright[5], Peter Teuben[6], Stuartt A. Corder[2,7], Jenny Patience[2,8], Nick Scoville[2], Jennifer Donovan Meyer[1], and Fumi Egusa[2]

[1] Department of Physics and Astronomy, Stony Brook University, Stony Brook, NY 11794-3800, USA; jin.koda@stonybrook.edu
[2] Department of Astronomy, California Institute of Technology, Pasadena, CA 91125, USA
[3] Joint ALMA Office, Alonso de C'ordova 3107, Vitacura, Santiago 763-0355, Chile
[4] National Astronomical Observatory of Japan, Mitaka, Tokyo 181-8588, Japan
[5] Department of Astronomy and Radio Astronomy Laboratory, University of California, Berkeley, CA 97420, USA
[6] Department of Astronomy, University of Maryland, College Park, MD 20742, USA
[7] North American ALMA Science Center, 520 Edgemont Road, Charlottesville, VA 22903, USA
[8] School of Physics, University of Exeter, Stocker Road, Exeter, EX4 4QL Devon, UK
Received 2010 November 9; accepted 2011 February 1; published 2011 March 3

ABSTRACT

We report the CO($J = 1$–0) observations of the Whirlpool Galaxy M51 using both the Combined Array for Research in Millimeter Astronomy (CARMA) and the Nobeyama 45 m telescope (NRO45). We describe a procedure for the combination of interferometer and single-dish data. In particular, we discuss (1) the joint imaging and deconvolution of heterogeneous data, (2) the weighting scheme based on the root-mean-square (rms) noise in the maps, (3) the sensitivity and uv coverage requirements, and (4) the flux recovery of a combined map. We generate visibilities from the single-dish map and calculate the noise of each visibility based on the rms noise. Our weighting scheme, though it is applied to discrete visibilities in this paper, should be applicable to grids in uv space, and this scheme may advance in future software development. For a realistic amount of observing time, the sensitivities of the NRO45 and CARMA visibility data sets are best matched by using the single-dish baselines only up to 4–6 $k\lambda$ (about 1/4–1/3 of the dish diameter). The synthesized beam size is determined to conserve the flux between the synthesized beam and convolution beam. The superior uv coverage provided by the combination of CARMA long baseline data with 15 antennas and NRO45 short spacing data results in the high image fidelity, which is evidenced by the excellent overlap between even the faint CO emission and dust lanes in an optical *Hubble Space Telescope* image and polycyclic aromatic hydrocarbon emission in a *Spitzer* 8 μm image. The total molecular gas masses of NGC 5194 and 5195 ($d = 8.2$ Mpc) are $4.9 \times 10^9\ M_\odot$ and $7.8 \times 10^7\ M_\odot$, respectively, assuming the CO-to-H_2 conversion factor of $X_{\rm CO} = 1.8 \times 10^{20}\ {\rm cm}^{-2}({\rm K\ km\ s}^{-1})^{-1}$. The presented images are an indication of the millimeter-wave images that will become standard in the next decade with CARMA and NRO45, and the Atacama Large Millimeter/Submillimeter Array.

Key words: galaxies: individual (NGC 5194, NGC 5195, M51) – techniques: image processing – techniques: interferometric

Online-only material: color figures

1. INTRODUCTION

Interferometers have an intrinsic limitation, namely, the problem of missing information. An interferometer records the target Fourier components of the spatial emission distribution, but an interferometer with a small number of antennas (N) can collect only a limited number, $N(N-1)/2$, of the Fourier components instantaneously. In addition, the finite diameter of each antenna limits the minimum separation between antennas, which, in turn, imposes a maximum size on an object that the interferometer can detect. The zero-spacing data (i.e., zero antenna separation data) carry the important information of the total flux, and this information is always missing. The incomplete Fourier coverage (uv coverage) also degrades the quality of the image. Deconvolution schemes have been developed to extrapolate the observed uv data to estimate the missing information, however, the performance is poor for objects with high contrast, such as spiral arms and the interarm regions of galaxies.

The small-N problem is particularly severe in millimeter astronomy, though it is greatly reduced with the 15 element Combined Array for Research in Millimeter Astronomy (CARMA). CARMA combines the previously independent Owens Valley Millimeter Observatory (OVRO) array ($N = 6$) and Berkeley–Illinois–Maryland Association (BIMA) array ($N = 10$—reduced to 9 for CARMA). The number of antenna pairs, or *baselines*, is increased to 105 from the previous values of 15 (OVRO) and 45 (BIMA), providing a substantial improvement in uv coverage. In most observatories, a few array configurations are used to increase the number of baselines. The uv coverage from one CARMA configuration is equivalent to that from seven configurations with a six-element array. CARMA ensures the unprecedented uv coverage in millimeter interferometry compared with previous millimeter-wave arrays.

Single-dish telescopes complement the central uv coverage and provide short baselines, including the zero-spacing baseline. The combination of interferometer and single-dish data is not trivial, though several methods have been suggested. Existing methods can be categorized into three types. The first method produces visibilities from a single-dish map (Vogel et al. 1984; Takakuwa 2003) and adds single-dish and interferometer data in the uv domain. Pety & Rodríguez-Fernández (2010) discussed a mathematical formalism. One issue faced when utilizing this method, the difficulties of which are discussed in Helfer et al. (2003), has been the weighting of the two sets of data in combination. Rodríguez-Fernández et al. (2008)

and Kurono et al. (2009) manually set the single-dish weight relative to the weight of the interferometer to improve the shape of the synthesized beam. In this paper, we suggest a new weighting scheme based solely on the quality of the single-dish data. In our method, the single-dish weight is independent of the interferometer data and is intrinsic to the single-dish observations. It naturally down-weights (up-weights) the single-dish data when its quality is poor (high). In Appendix C, we discuss the sensitivity matching that makes the combination most effective.

The second type of combination method co-adds two sets of data in the image domain (Stanimirovic et al. 1999). This approach produces a joint dirty image and synthesized beam[9] by adding the single-dish map and the interferometer dirty image, and single-dish beam and interferometer synthesized beam, respectively. The joint dirty image is then deconvolved with the joint dirty beam. This technique was adopted for the BIMA-SONG survey (Helfer et al. 2003). Cornwell (1988), and recently Stanimirovic et al. (2002), also discussed a nonlinear combination technique through joint deconvolution with the maximum entropy method (MEM).

The third method was introduced by Weiß et al. (2001) and operates in the Fourier plane. The deconvolved interferometer map and single-dish map are Fourier transformed and then the central uv space from interferometer data is replaced with single-dish data.

This paper describes the observations, data reduction, and combination of CARMA and Nobeyama Radio Observatory 45 m telescope (NRO45) data of M51. Our procedure unifies the imaging techniques for interferometer mosaic data, heterogeneous array data, and the combined data of the single-dish and interferometer. Earlier data reduction and results have been published (Koda et al. 2009). The method and results are the same, but we have re-calibrated and reduced the entire data set using higher accuracy calibration data. In Sections 2 and 3, we describe the CARMA and NRO45 observations and calibration. The deconvolution (such as CLEAN) is detailed in Section 4 for three cases: (1) homogeneous array, single-pointing observations, (2) heterogeneous array, single-pointing observations, and (3) heterogeneous array, mosaic observations. The weighting scheme in co-adding the images from a heterogeneous array (with multiple primary beams) is discussed in Section 4.4. The result from this subsection is also essential for the combination of interferometer and single-dish data. The conversion of a single-dish map to visibilities is explored in Section 5, and Section 6 discusses the resultant map and image fidelity. A summary of the requirements of single-dish observations for the combination is explained in Section 7. Comments on other combination methods are given in Section 8. The summary is in Section 9, and sensitivity matching between single-dish and interferometer observations is discussed in Appendix C.

2. CARMA

2.1. Observations

High-resolution observations of the Whirlpool galaxy M51 in the CO(J = 1–0) line were performed with CARMA during the commissioning phase and in the early science phase during the CARMA construction (2006–2007). CARMA is a recently developed interferometer, combining the six 10 m antennas of the Owens Valley Radio Observatory (OVRO) millimeter interferometer and the nine 6 m antennas of the BIMA interferometer. The increase to 105 baselines provides superior uv coverage and produces high image fidelity. The C and D array configurations are used. The baseline length spans over 30–350 m (C array) and 11–150 m (D array).

The observations started with the heterodyne superconductor–insulator–superconductor (SIS) receivers from OVRO and BIMA. The typical system temperature of these original receivers was ∼200 K in double-side band (DSB). The receivers of the 15 antennas were being upgraded one antenna at a time during the period of observations, but the process was not completed before these observations finished. The system temperature of the new receivers is typically ∼100 K at 115 GHz.

The first-generation CARMA digital correlators were used as a spectrometer. They had three dual bands (i.e., lower and upper side bands) for all 105 baselines. Each band had five configurations of bandwidth—500, 62, 31, 8, and 2 MHz—which have 15, 63, 63, 63, and 63 channels, respectively. We switched the configuration of bands 1, 2, 3 between (bands 1, 2, 3) = (500, 500, 500) for gain calibration quasar observations and (bands 1, 2, 3) = (62, 62, 62) for target integrations. This "hybrid" configuration ensures both a sufficient detection of the gain calibrator 1153+495 with the total 3 GHz bandwidth (i.e., 3 bands × 2 side bands × 500 MHz bandwidth) and a sufficiently wide velocity coverage for the main galaxy NGC 5194. The total bandwidth is 149.41 MHz after dropping edge six channels at each side, which could be noisier than the central channels. The companion galaxy NGC 5195 was not included in the velocity coverage, although it was detected in the NRO45 map (Section 3.1).

The hybrid mode observations require a special calibration for amplitude and phase offsets between bands and between configurations. We observed a bright quasar by changing the correlator configurations in time sequence: (1) (bands 1, 2, 3) = (500, 500, 500), (2) (62, 62, 62), (3) (500, 62, 62), (4) (62, 500, 62), and (5) (62, 62, 500). Each configuration spends 5 minutes on integration, and the whole sequence takes 25 minutes for integration in total. We used the bright quasars 3C273, 2C279, or 3C345, depending on availability during the observations. For any pair of band and bandwidth, this sequence has simultaneous integrations which can be used to calibrate the phase offset and amplitude scale between bands. The calibration observations typically took 45 minutes including the radio pointing and antenna slew. These integrations were used for passband calibration as well.

An individual observation consisted of a 4–10 hr track. The total observing time (after flagging tracks under bad weather) is about 230 hr (∼30 tracks). A typical track starts with radio pointing observations of a bright quasar available at the time, then observes a flux calibrator (e.g., a planet), and repeats the 25 minute observing cycle of the gain calibrator (∼5 minutes) and target (20 minutes including antenna slew for mosaic). The passband/hybrid observations were performed at the middle of a track when M51 was at a high elevation (∼80°). At such a high elevation, each antenna slew between M51 and the calibrator takes a considerable amount of time. Observing a passband calibrator at a lower elevation avoids this loss. The system temperature ($T_{\rm sys}$) was measured every gain calibrator cycle, and the atmospheric gain variation is corrected real time using $T_{\rm sys}$. We observed 1153+495 as a gain calibrator.

The telescope pointings were corrected every 4 hr during the night and every 2 hr during daytime. The last ∼10 tracks of the 30 total tracks also included an additional optical pointing

[9] The synthesized beam is the instrumental point-spread function for the aperture synthesis array; also known as the "dirty beam."

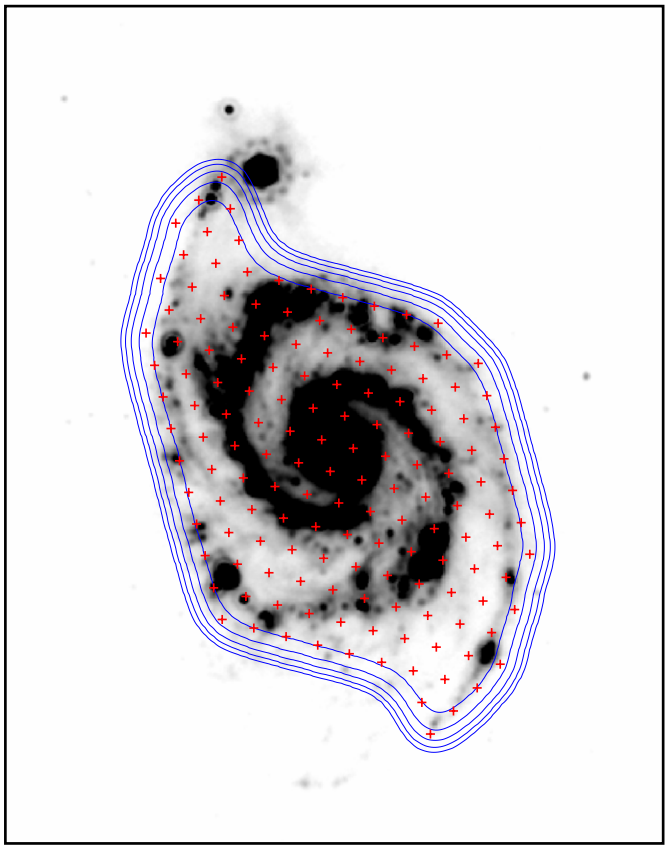

Figure 1. Observed areas of M51 over the *Spitzer* 24 μm image of M51. Red crosses: 151 pointing positions of CARMA observations. Blue contours: sensitivities (rms noise) of 120%, 140%, 160%, 180%, and 200% with respect to the central maximum sensitivity. Most part over the galactic disk has a uniform sensitivity. Black box: NRO45 coverage.

(A color version of this figure is available in the online journal.)

procedure developed by Corder et al. (2010). The optical procedure can operate during daytime, as well as at night, and a pointing correction was made every gain calibration cycle. This method measures the offset between radio and optical pointing vectors at the beginning of track (which is stable over periods much longer than the typical observation). During the observing cycle of the gain calibrator and target, the pointing drift, typically several arcseconds per hour, is adjusted using a bright star close to the gain calibrator using an optical camera. The overhead of the pointing adjustment is less than 1 minute.

We mosaicked the entire $6\farcm0 \times 8\farcm4$ disk of M51, with the disk defined by optical images and shown in Figure 1, in 151 pointings with Nyquist sampling of the 10 m antenna beam (FWHM of 1 arcmin for the 115 GHz CO $J = 1$–0 line). Ideally, every pointing position would be observed every M51 observing cycle (~20 minute duration) to maintain uniform data quality and uv coverage across the mosaicked area. However, the overhead for slewing is significant for the large mosaic. It is as long as 6 s per slew, and about 15 minutes total for 151 pointings. We therefore observed every third pointing (total ~50 pointings) in each observation cycle to reduce the overhead. Three consecutive cycles cover all 151 pointings. Each track started from a pointing randomly chosen from the table of the 151 pointings, which helps the uniform data quality among pointings. The resultant CARMA uv coverage is very similar at all pointings, and an example of the uv coverage at the central pointing is in Figure 2.

The primary flux calibrators, Uranus, Neptune, and MWC349, were observed in most tracks. We monitored the flux of gain calibrator 1153+495 every month over the course of the observations. The flux of 1153+495 varied slowly between 0.7 and 1.3 Jy. The CARMA observatory is separately monitoring the flux variations of common passband calibrators, and our flux measurements are consistent with the observatory values.

2.2. Calibration

The data were reduced and calibrated using the Multichannel Image Reconstruction, Image Analysis, and Display (MIRIAD) software package (Sault et al. 1995). We developed additional commands/tasks to investigate and to reduce the large amount of data effectively, and to combine interferometer and single-dish data.

The initial set of calibrations are the required routines for most CARMA data reductions. First, we flag the data with problems such as antenna shadowing and bad $T_{\rm sys}$ measurements. Second, we apply the correction for variation of optical fiber cable length, namely line-length correction. CARMA is a heterogeneous array of two types of antennas (i.e., 6 m and 10 m), and the optical fiber cables that connect the antennas to the control building are mounted differently for the 10 m and 6 m dishes. The time variations of the cable lengths due to thermal expansion are therefore different, which results in phase wraps in the baselines between 6 m and 10 m antennas. The changes of the cable lengths were monitored to an accuracy of 0.1 ps by sending signals from the control building and measuring their round-trip travel time. The changes are stored in MIRAD data and are used for the line-length correction. Third, we smooth the spectra with the Hanning window function to reduce the high sidelobes in raw spectra from the digital correlators. The spectral resolution is lowered by a factor of two and becomes 1.954 MHz (5.08 km s^{-1} at the CO($J = 1$–0) frequency).

Calibrations for the passband and hybrid correlator configurations were made using the sequence of hybrid configuration observations described in Section 2.1. We first separate 500 MHz and 62 MHz integrations from the sequence and generate two MIRIAD data sets containing only 500 MHz data or 62 MHz data. These data sets are used to derive and apply passbands. The passband calibration removes the phase and amplitude offsets among bands 1, 2, and 3 in the 500 and 62 MHz modes. An offset/passband calibrator is significantly detected even in a 10 s integration both in the 62 MHz and in the 500 MHz mode. We derive the phase offset and amplitude scale between the 500 MHz and 62 MHz modes by comparing the visibilities from the two modes on the 10 s integration basis, and averaging them over time to derive single values for the phase offset and amplitude scale. We applied these calibrations to the entire track, which removes the phase and amplitude offsets between gain calibrator and target integrations. Errors of the hybrid calibration are small compared with the other errors and are only a few percent in amplitude and a few degrees in phase.

The last set of calibrations includes the standard phase calibrations to compensate for atmospheric and instrumental phase drifts. We did not use the gain calibrator integrations with large phase scatters (due to bad weather) and flagged the target integrations in the cycles immediately before and after the bad gain data. The absolute fluxes of the gain calibrator were measured monthly against a planet (Section 2.1) and were applied to target data.

The resulting 1σ noise level of the CARMA data is 27 mJy beam^{-1} in each 10 km s^{-1} channel.

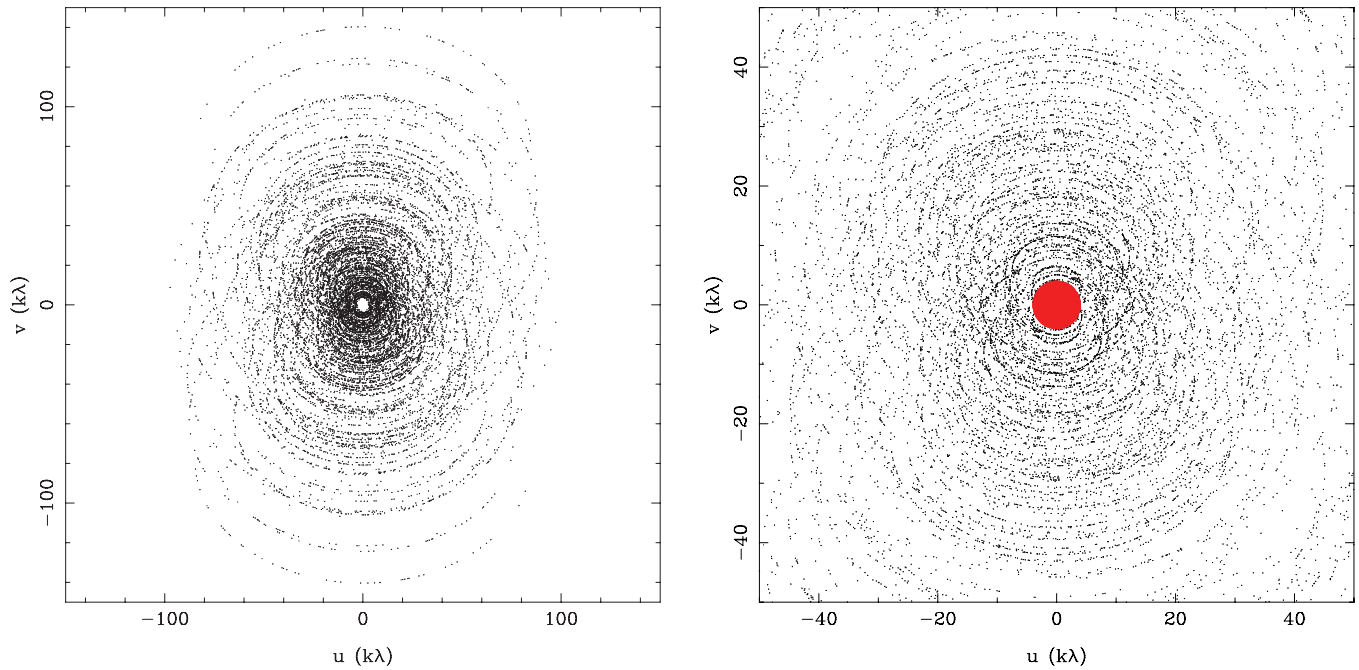

Figure 2. uv coverage at the central pointing in unit of kilo-lambda. Left: CARMA uv coverage. Right: the central region of CARMA (black) and NRO45 (red) uv coverages.

(A color version of this figure is available in the online journal.)

3. NOBEYAMA RADIO OBSERVATORY 45 m TELESCOPE

3.1. Observations

We obtained total power and short spacing data with the 5×5 Beam Array Receiver System (BEARS; Sunada et al. 2000) on the NRO45. The FWHM of the NRO45 beam is 15″ at 115 GHz. We configured the digital spectrometer (Sorai et al. 2000) to 512 MHz bandwidth at 500 kHz channel resolution. This is wide enough to cover the entire M51 system (both NGC 5194 and 5195). Hanning smoothing was applied to reduce the sidelobe in the channel, and therefore, the resolution of raw data is 1 MHz.

We scanned M51 in the R.A. and decl. directions using the On-The-Fly (OTF) mapping technique (Mangum et al. 2007; Sawada et al. 2008). We integrated OFF positions around the galaxy before and after each ∼1 minute OTF scan. A scan starts from an emission-free position at one side of the galaxy and ends on another emission-free position at the other side. Spectra are read out every 0.1 s interval during the scan. The receiver array was rotated by 7° with respect to the scan directions, so that the 25 beams draw a regular stripe with a 5″ separation. In combining the R.A. and decl. scans, the raw data form a lattice with 5″ spacing. This fine sampling, with respect to the beam size of 15″, is necessary in reproducing the uv data up to the 45 m baseline (i.e., the diameter of NRO45), since we need the Nyquist sampling (5.″96) of $\lambda_{\rm CO}/D = 11.''92$, where $\lambda_{\rm CO}$ is the wavelength (= 2.6 mm) and D is the antenna diameter (Mangum et al. 2007). If the sampling is coarser than 5.″96, the aliasing effect in the Fourier space significantly contaminates even shorter baseline data. For example, if the sampling spacing is only 10.″3 (i.e., typical sampling in past NRO45 observations; Kuno et al. 2007), the uv data down to the ∼7 m baseline are contaminated (Figure 3) and cannot be combined with the interferometer data.

The typical system temperature in DSB was ∼320 K. The pointing of the telescope was checked every ∼45 minutes and

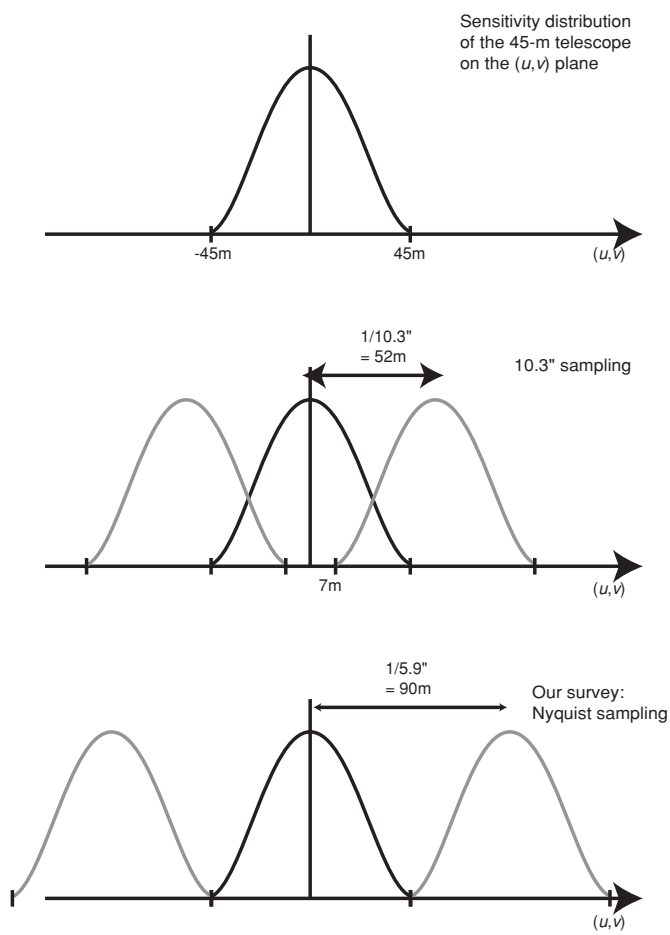

Figure 3. Schematic illustrations of the aliasing effect in the uv coverage of the NRO45 map. The alias of the NRO45 data in uv space destroys not only long, but also short baselines. In the case of 10.″3 sampling, the baselines as short as 7 m are affected by the alias.

was accurate to within ∼2″–3″. BEARS is an array of DSB receivers and provides the antenna temperature T_a^*(DSB) in DSB. The upper/lower side band ratio, namely the scaling factor, was measured by observing Orion IRC2 using both BEARS and the single-side band (SSB) receiver S100 and taking the ratios of the two measurements. The error in the measurements is a few percent. The total observing time under good weather conditions is about 50 hr.

3.2. Calibration

The ON/OFF calibration to account for the sky background level was applied after the observations. We interpolated between two OFF-sky integrations before and after each OTF scan (∼1 minute long), which reduced nonlinear swells in the spectral baselines significantly. We used the *NOSTAR* data reduction package developed at the Nobeyama Radio Observatory (Sawada et al. 2008), converted the flux scale from T_a^*(DSB) of BEARS to T_a^*(SSB) of S100, subtracted linear spectral baselines, and flagged bad integrations.

The 5″ lattice of data from the observations was re-gridded with a spheroidal smoothing function, resulting in a final resolution of 19″.7. We used the grid size of 5″.96, which is the Nyquist sampling of the 45 m spacing in Fourier space; this pixel scale is necessary to prevent artifacts from the aliasing effect (Section 3.1).

We made maps of the R.A. and decl. scans separately. The two maps were co-added after subtracting spatial baselines in each scan direction to reduce systematic errors in the scan direction. Note that for OTF mapping, the sharing of an OFF among many ON scans may introduce noise correlations, primarily at small spatial frequencies in the Fourier space. Emerson & Gräve (1988) reduced such correlated noise using the basket-weave method, which down-weights the data at small spatial frequencies in the scan directions when the R.A. and decl. maps are added. We compared the spatial-baseline subtraction and basket-weave methods, and found that both diminish the large-scale noise well. The difference was subtle, but the former gave a slightly smaller rms noise, and thus, we decided to use the spatial-baseline method.

The antenna temperature T_a^*(SSB) was converted to the main beam temperature $T_{\rm mb}$, using the main beam efficiency of $\eta_{\rm mb} = 0.4$ and $T_{\rm mb} = T_a^*({\rm SSB})/\eta_{\rm mb}$.

The flux of the final NRO45 map is consistent with most previous measurements within a typical error of millimeter-wave measurements (10%–20%). It is compared with four other results: an image from the National Radio Astronomy Observatory 12 m telescope (NRAO12; Helfer et al. 2003), two previous measurements at NRO45 (Nakai et al. 1994; Matsushita et al. 1999), and our new CARMA data (Section 2). The fluxes from Helfer et al. (2003), Matsushita et al. (1999), and the new CARMA observations are 94%, 95%, and 93% of that of the new NRO45 map, respectively. For the comparisons, we re-sampled the new map to match the area coverage of the other maps. For the comparison with CARMA, the CARMA uv distribution is generated from the new NRO45 map (as discussed in Section 5.1, but for Hatcreek, OVRO, and CARMA primary beams), and the positive fluxes (above about 4σ) in the dirty maps are compared to measure the flux ratio. We used a Gaussian taper (FWHM = 20″) to make the dirty maps, which roughly reproduces the weight distribution of the NRO45 data.

Only the map of Nakai et al. (1994, distributed through Kuno et al. 2007) shows a significant discrepancy: a factor of 1.82 higher total flux than the new NRO45 map. We attribute this discrepancy to an error in the old map, since all other measurements are consistent. Among these measurements, we decided to rely on the CARMA flux because we had the best understanding of the process of flux calibration, and because it is based on multiple flux calibrations over the duration of the observations. We scaled the flux of the NRO45 map to match the CARMA flux (i.e., multiplied 0.93).

The 1σ noise level of NRO45 data is 14.7 mK in T_a^*(SSB), 36.7 mK in $T_{\rm mb}$, and 155 mJy beam^{-1} in 10 km s^{-1} channel.

4. IMAGING HETEROGENEOUS-ARRAY MOSAIC DATA

We use MIRIAD for joint deconvolution of multi-pointing CARMA and NRO45 data. The method and algorithm for mosaic data with a homogeneous array are described in Sault et al. (1996). Our imaging involves two additional complications: a heterogeneous array, and combinations with single-dish data, as well as mosaicking. We describe the essence of joint deconvolution using MIRIAD, with an emphasis on the case of CARMA and NRO45.

Two points are of particular importance: the treatment of different primary beam patterns, and the weights of the data from the different primary beam patterns and from the single dish. Here, we illustrate these two points and define our notations.

Correction for primary beam attenuation is simple for a homogeneous array. All antennas have the same primary beam pattern $P(l, m)$, and the primary-beam correction is

$$I(l, m) = \frac{\bar{I}(l, m)}{P(l, m)}, \tag{1}$$

where the primary-beam corrected image is denoted as I and the uncorrected image is denoted as $\bar{I}$. The sky coordinates are (l, m). The uncorrected image $\bar{I}$ has two advantages: the synthesized beam $\bar{B}$ (i.e., point-spread function, PSF) and noise level are position invariant, which simplifies the process of deconvolution (Section 4.1).

For a heterogeneous array, the differences between primary beam patterns have to be taken into account. For example, CARMA has three baseline types (i.e., antenna pairs), which result in three primary beam patterns—called "H" for Hatcreek (6 m–6 m dish pair), "O" for OVRO (10 m–10 m), and "C" for CARMA baseline types (6 m–10 m). Using appropriate weights $W_{\rm H}$, $W_{\rm O}$, and $W_{\rm C}$ (Section 4.4), the images from "O," "H," and "C" baselines can be added as

$$\begin{aligned} I(l, m) &= W_{\rm H}\frac{\bar{I}_H}{P_{\rm H}} + W_{\rm O}\frac{\bar{I}_O}{P_{\rm O}} + W_{\rm C}\frac{\bar{I}_C}{P_{\rm C}} \\ &= W_{\rm H} I_H + W_{\rm O} I_O + W_{\rm C} I_C. \end{aligned} \tag{2}$$

The weight W is a function of position (l, m). The co-added image has been corrected for primary beam attenuation. In the co-added plane, the synthesized beam pattern B and noise level are position variant, which complicates the deconvolution.

4.1. Homogeneous Array, Single-pointing Data

Traditionally, the imaging of interferometer data has been performed as follows. A set of *one* dirty map $\bar{I}^{\rm dm}(l, m)$ and *one* synthesized beam pattern $\bar{B}(l, m)$ is made from visibilities. The dirty map $\bar{I}^{\rm dm}$ is deconvolved with $\bar{B}$. For example, the deconvolution scheme CLEAN replaces the pattern $\bar{B}(l - l_0, m - m_0)$, centered at an emission peak at (l_0, m_0), with an ellipsoidal Gaussian to reduce the sidelobes of $\bar{B}$. CLEAN usually

runs in the $\bar{I}^{\rm dm}$ domain; the synthesized beam $\bar{B}$ and noise level σ are position invariant and their treatments are simple. The CLEANed image $\bar{I}^{\rm mp}$ is corrected for primary beam attenuation (Equation (1)), providing the final map $I^{\rm mp}$. We note again that primary beam uncorrected and corrected images (of any kind) are differentiated with "bar" (e.g., $\bar{I}^{\rm dm}$ versus $I^{\rm dm}$ and $\bar{I}^{\rm mp}$ versus $I^{\rm mp}$).

The deconvolution is also possible in the $I^{\rm dm}$ domain. The synthesized beam pattern B and noise level are *not* position invariant. Thus, we define a position-variant synthesized beam pattern,

$$B(l, m; l_0, m_0) = \frac{\bar{B}(l - l_0, m - m_0)}{P(l, m)}, \tag{3}$$

centered at (l_0, m_0), and a position-variant noise level $\sigma/P(l, m)$. Emission peaks are searched on a basis of signal-to-noise ratio. In MIRIAD, a set of primary-beam corrected I and uncorrected $\bar{B}$ values is calculated from visibilities, and the command "mossdi" (i.e., CLEAN) calculates B with Equation (3) at the peak position (l_0, m_0).

4.2. Heterogeneous Array, Single-pointing Data

The deconvolution in the image domain is applicable to heterogeneous array data. The joint dirty image $I^{\rm dm}$ is defined as a linear summation of three dirty maps $I^{\rm dm}_{\rm H}$, $I^{\rm dm}_{\rm O}$, and $I^{\rm dm}_{\rm C}$ (Equation (2)). The corresponding synthesized beam B is also a linear summation with the same weights,

$$\begin{aligned} B(l, m; l_0, m_0) = {} & W_{\rm H}(l, m)\frac{\bar{B}_H(l - l_0, m - m_0)}{P_H(l, m)} \\ & + W_{\rm O}(l, m)\frac{\bar{B}_O(l - l_0, m - m_0)}{P_O(l, m)} \\ & + W_{\rm C}(l, m)\frac{\bar{B}_C(l - l_0, m - m_0)}{P_C(l, m)}. \end{aligned} \tag{4}$$

The MIRIAD command "invert" with the mosaic option outputs a set of *one* joint dirty map $I^{\rm dm}$ (primary-beam corrected) and *three* synthesized beams $\bar{B}_{\rm H}$, $\bar{B}_{\rm O}$, and $\bar{B}_{\rm C}$ (uncorrected). The command "mossdi" finds a peak emission in $I^{\rm dm}$ and calculates B at its position with Equation (4).

In the case of a heterogeneous array, such as CARMA, the primary-beam correction always needs to be applied to the dirty map. Thus, even for single-pointing observations, we always use "options=mosaic" for "invert."

4.3. Heterogeneous Array, Mosaic Data

The deconvolution of mosaic data with a heterogeneous array is a further extension of the same procedure. Equation (2) is extended as

$$I(l, m) = \sum_{b,p} W_{b,p}\frac{\bar{I}_{b,p}}{P_{b,p}} = \sum_{b,p} W_{b,p} I_{b,p}, \tag{5}$$

where the summation is taken for all baseline types b and pointings p. $W_{b,p}$ is a weight for b and p. In practice, P is truncated at some radius, and only a subset of pointings contribute to a given position.

The joint synthesized beam is defined as in Equation (4), but includes all pointings. In the case of the CARMA M51 observations, the command "invert" with "option=mosaic" outputs 1 joint dirty map and 453 synthesized beams (=3 baseline types × 151 pointings). A joint synthesized beam B is calculated with the 453 synthesized beams for every emission peak in $I^{\rm dm}$.

The spatial resolution is calculated by taking a weighted average of all 453 synthesized beams using W_b (b = H, O, C) and by fitting a Gaussian. In theory, the sizes of the synthesized beams are different among the pointings, since the uv coverage is not exactly the same for all of the pointings. In practice, we designed the observations to provide uniform uv coverage for all pointings (Section 2.1). We therefore adopt a single beam size over the whole mosaic.

4.4. Weighting

The noise level is position dependent, $\sigma/P(l, m)$, in the image domain. Therefore, the weights W are defined as

$$W_b(l, m) \propto \left(\frac{P_b(l, m)}{\sigma}\right)^2 \tag{6}$$

for b = H, O, and C, and are normalized as $W_{\rm H}+W_{\rm O}+W_{\rm C} = 1$ at each position (l, m). The theoretical noise σ depends on baseline type b and is the same as the imaging sensitivity $\Delta S^{\rm i}$ discussed below.

4.4.1. Thermal Noise and its Coefficient

Two sensitivities, fringe sensitivity $\Delta S^{\rm f}$ and imaging sensitivity $\Delta S^{\rm i}$ [$\equiv \sigma$], are important (Wrobel & Walker 1999, see their Section 9). The fringe sensitivity is a sensitivity per visibility. The theoretical sensitivity $S^{\rm f}$ for each visibility is calculated with the system temperature $T_{\rm sys}$, bandwidth B, and integration time of the visibility $t_{\rm vis}$ as

$$\Delta S^{\rm f} = C_{ij}\sqrt{\frac{T_{{\rm sys},i}T_{{\rm sys},j}}{B \cdot t_{\rm vis}}}, \tag{7}$$

where

$$C_{ij} = \frac{2k_{\rm B}}{\sqrt{(\eta_{a,i}A_i)(\eta_{a,j}A_j)}}\frac{1}{\sqrt{2}\eta_q}. \tag{8}$$

The aperture efficiency η_a and collecting area A of antennas i and j have a relation with the beam solid angle $\Omega_{\rm A}$ given by $1/(\eta_a A) = \Omega_{\rm A}/\lambda^2$. The Boltzmann constant is $k_{\rm B}$ and the last term $1/\sqrt{2}\eta_q$ is due to the backend (i.e., digitizer and correlator), and η_q is the quantum efficiency (Rohlfs & Wilson 2000). C_{ij} is approximated as a constant for a homogeneous array, since the parameters are very similar for all antennas. In the case of a heterogeneous array, C_{ij} depends on baseline type. Parameters are listed in Table 1.

The imaging sensitivity is a root-mean-square (rms) noise in a final image and depends on control parameters (see Appendix A; e.g., natural and uniform weighting). If the natural weighting is employed, the imaging sensitivity is simply a statistical summation of fringe sensitivities, $1/(\Delta S^{\rm i})^2 = \Sigma_k 1/(\Delta S^{\rm f})^2$. For a homogeneous array (C_{ij} is constant), it is

$$\Delta S^{\rm i}[\equiv \sigma] = C_{ij}\sqrt{\frac{T_{{\rm sys},i}T_{{\rm sys},j}}{B \cdot t_{\rm tot}}}, \tag{9}$$

assuming that $T_{\rm sys}$ is a constant during observations. The total integration time is $t_{\rm tot} = N_{\rm vis}t_{\rm vis}$, where $N_{\rm vis}$ is the number of visibilities.

Table 1
Antenna Parameters at 115 GHz

Parameter		Unit	Hatcreek (6 m)	OVRO (10 m)	CARMA (6 m–10 m)	NRO45
Main beam size	FWHM	arcsec	100	60	77.5[a]	19.7[b]
Beam solid angle	Ω_b	arcsec^2	1.51×10^4	6.77×10^3	1.01×10^4 [a]	1.10×10^3 [b]
Quantum efficiency	η_q	···	0.87	0.87	0.87	0.87
Main beam efficiency	η_{mb}	···	0.41	0.61	0.50[a]	0.40
Noise coef. (general)	C_{ij}	Jy K^{-1}	116.8	52.2	78.1[a]	12.0
Noise coef. (MIRIAD)	JYPERK	Jy K^{-1}	145.3	65.0	97.2[a]	14.9

Notes.
[a] Geometric mean of Hatcreek and OVRO values.
[b] After re-gridding (Section 3.2).

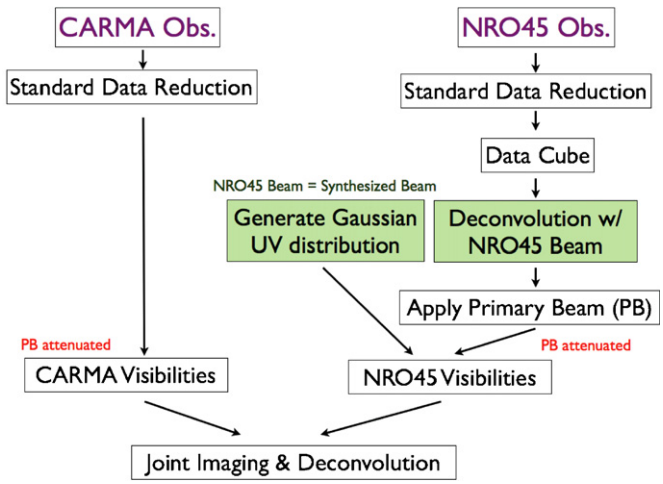

Figure 4. Flow chart of the process of combination. The NRO45 cube is deconvolved with the NRO45 beam, multiplied with an arbitrarily selected primary beam, and Fourier-transformed into uv space. The transformed data are re-sampled with a Gaussian uv distribution to produce NRO45 visibilities. The weight of the NRO45 visibilities, with respect to CARMA, is determined based on the rms noise of the NRO45 cube.

(A color version of this figure is available in the online journal.)

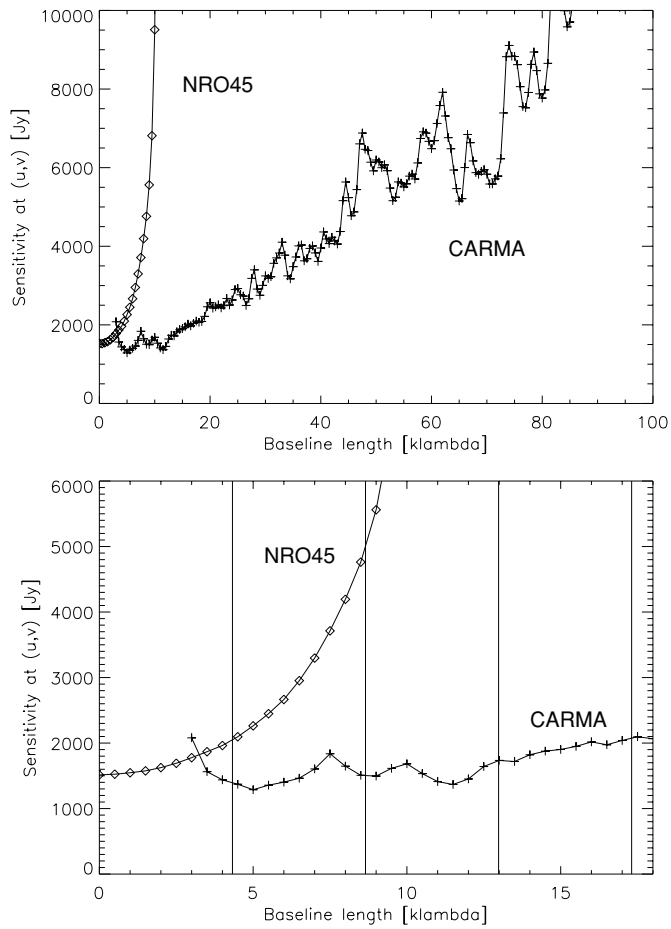

Figure 5. Sensitivities as a function of baseline length for NRO45 (diamonds) and CARMA (crosses). The bottom panel is the same as the top panel, but only for short baselines. Vertical lines, from right to left, correspond to the antenna diameter of NRO45 (45 m) and its three quarter, half, and quarter lengths.

5. THE COMBINATION OF NRO45 WITH CARMA

The NRO45 image is converted to visibilities and combined with CARMA data in uv space. Here we discuss four steps for combination: (1) generating visibilities from the single-dish image, (2) the calculation of the weights of the single-dish visibilities, in the same form as interferometer visibilities, (3) the determination of synthesized beam size, and (4) an imaging/deconvolution scheme. A flow chart of the procedure is shown in Figure 4.

5.1. Converting the NRO45 Map to Visibilities

To produce NRO45 visibilities, we first deconvolve an NRO45 map with an NRO45 PSF, multiply a dummy primary beam, generate a Gaussian visibility distribution, and calculate the amplitude and phase of the visibilities from the deconvolved, primary-beam applied NRO45 map (Figure 4). The following subsections describe these steps.

One limitation arises from the current software, though it should be easily modified in future software development. NRO45 visibilities must have the same form as those of interferometers, and therefore, a dummy primary beam needs to be applied to the NRO45 map.

5.1.1. Deconvolution with the NRO45 Beam

A NRO45 map is a convolution of a true emission distribution with a PSF. In the case of OTF mapping (Section 3.1), the PSF is not literally the NRO45 beam, but is a convolution of the NRO45 beam and the spheroidal function that is used to re-grid the observed data to a map grid (Section 3.2). The intrinsic Gaussian FWHM of the NRO45 beam is 15″ and is degraded to 19″.7 after the re-gridding. The NRO45 map needs to be deconvolved with this PSF.

Figure 5 shows the sensitivity (noise) as a function of uv distance (baseline length). It has a dependence on the Fourier-transformed PSF FT{PSF} as $\propto 1/\sqrt{\mathrm{FT\{PSF\}}}$ (see

Appendix C). The standard deviation of FT{PSF} is $\sigma_F = 3.9$ kλ for a Gaussian PSF with the FWHM of 19″.7. Thus, the noise increases significantly beyond 4–6 kλ (i.e., $\sqrt{2}\sigma_F$). Figure 5 shows that the NRO45 sensitivity is comparable to that of CARMA up to 4–6 kλ and deviates beyond that. With the resultant sensitivities, we decided to flag the data at >4 kλ. The long baselines have negligible effects if we use the weight based on sensitivity (i.e., robust = +2; Briggs 1995), but could introduce an elevated error when robust < +2.

CARMA and NRO45 are complementary in terms of uv coverage and sensitivity (Figures 2 and 5). Kurono et al. (2009) suggested that the single-dish diameter should be 1.7 times as large as the minimum baseline of interferometer data, which is ∼18 m in our case. However, we seem to need a 45 m class telescope to satisfy the sensitivity requirement within realistic observing time. The sensitivity matching between NRO45 and CARMA data is discussed in Appendix C.

5.1.2. Applying a Dummy Primary Beam

The imaging tasks in MIRIAD assume that all visibilities are from interferometric observations and apply a primary-beam correction in the process of imaging. Consequently, the NRO45 visibilities need to be attenuated by a pseudo primary beam pattern P_N. The choice of P_N is arbitrary, and we employ a Gaussian primary beam with the FWHM of 2 arcmin. P_N is multiplied to the deconvolved NRO45 map at each of the 151 CARMA pointings separately. Since the map will be divided by P_N during the deconvolution, the choice of P_N does not affect the result. However, it is safer to use a P_N value that is at least twice as large as the separation of the pointings, so that the entire field is covered at the Nyquist sampling (or oversampling) rate.

We note that this multiplication of a primary beam in the image domain is equivalent to a convolution in the Fourier domain. It smoothes the sensitivity distribution in uv space, and therefore, the weight discussed in Section 5.2. The size of the primary beam in Fourier space is only 1/6 of that of the NRO45 beam. Therefore, this effect should be small and negligible.

5.1.3. Generating a Gaussian Visibility Distribution

The distribution of visibilities in uv space should reproduce the NRO45 beam (more precisely, the PSF in Section 5.1) as a synthesized beam in image space. The Fourier transformation of a Gaussian PSF is a Gaussian. Therefore, visibilities are distributed to produce a Gaussian density profile in uv space. The size of the Gaussian distribution is set to reproduce the beam size of 19″.7. We manually add a visibility at $(u, v) = (0, 0)$, so that the zero spacing is always included. The number of visibilities $N_{\rm vis}$ and integration time per visibility $t_{\rm int}$ are control parameters and are discussed in Section 5.2.

5.1.4. Resampling

From the Gaussian visibility distribution and the primary beam attenuated maps, the visibility amplitudes and phases are derived, which gives the NRO45 visibilities.

5.2. Theoretical Noise and Other Parameters

The relative weights of the CARMA and NRO45 visibilities are important for proper combination. MIRIAD requires a weight (sensitivity) per individual visibility for imaging, and we calculate the weight based on the rms noise of an NRO45 map. For the interferometer data (Section 4.4.1), we start from the fringe sensitivity $S^{\rm f}$ and calculate the imaging sensitivity $S^{\rm i}$ by summing up the $S^{\rm f}$s of all visibilities. Here, we start from the rms noise of a map (i.e., $S^{\rm i}$) and determine $S^{\rm f}$ and its coefficient.

The theoretical noise of a single-dish map, in main beam temperature $T_{\rm mb}$, is

$$\Delta T_{\rm mb} = \frac{T_{\rm sys}}{\eta_q \eta_{\rm mb}\sqrt{B \cdot t_{\rm tot}}}, \tag{10}$$

where η_q and $\eta_{\rm mb}$ are the quantum efficiency of the spectrometer and the main beam efficiency of the antenna, respectively. B and $t_{\rm tot}$ are the bandwidth and total integration time, respectively. (Note that the contribution to the noise from the OFF position integrations should be negligible in OTF mapping (Sawada et al. 2008)). The total integration time (per point) of the NRO45 map is derived from the rms noise in the map using this equation.

The imaging sensitivity, corresponding to Equation (9), is calculated by converting the units of Equation (10) from K to Jy,

$$\Delta S^{\rm i} = \frac{2k_{\rm B}}{\eta_a A}\frac{T_{\rm sys}}{\eta_q \eta_{\rm mb}\sqrt{B \cdot t_{\rm tot}}}. \tag{11}$$

Comparing with Equation (9), we obtain

$$C_{ij} = \frac{2k_{\rm B}}{\eta_{\rm mb}\eta_a A}\frac{1}{\eta_q}. \tag{12}$$

The fringe sensitivity per visibility should be

$$\Delta S^{\rm f} = C_{ij}\frac{T_{\rm sys}}{\sqrt{B \cdot t_{\rm vis}}}, \tag{13}$$

where the integration time per visibility is $t_{\rm vis} = t_{\rm tot}/N_{\rm vis}$ and $N_{\rm vis}$ is the number of visibilities. The $t_{\rm vis}$ value should be set (arbitrary) to a small number, so that $N_{\rm vis}$ becomes large enough to fill the uv space. We set $t_{\rm vis} = 0.01$ s and $N_{\rm vis} = 42075$.

Conceptually, we can understand the meaning of the NRO45 visibilities by comparing the definitions of fringe sensitivities (Equations (7) and (13)). They are the ones observed virtually with two identical NRO45 antennas. The two antennas can physically overlap (in our virtual observations), so they can provide uv coverage down to zero spacing. The beam shape of the NRO45 dish plays the role of synthesized beam, but not the role of primary beam. The primary beam shape is arbitrarily defined by P_N—if we seek a meaning, it corresponds to the beam shape of small patches within the NRO45 dishes.

There is one caveat when this weighting method is applied with the current version of MIRIAD. MIRIAD is designed for an array with the same backend for all visibilities, and therefore, it neglects the $1/\sqrt{2}\eta_q$ term from C_{ij} (Equation (8)). It defines an alternative parameter,

$$\text{JYPERK} = \frac{2k_{\rm B}}{\sqrt{(\eta_{a,i}A_i)(\eta_{a,j}A_j)}}, \tag{14}$$

which is stored in data header. The weights ($\Delta S^{\rm f}$) are calculated with JYPERK, instead of C_{ij}, and do not take into account the backend. In combining CARMA data with single-dish data, we can overwrite JYPERK in CARMA data with C_{ij}, or define JYPERK for single dish (NRO45), as

$$\text{JYPERK} = \frac{2\sqrt{2}k_{\rm B}}{\eta_{\rm mb}\eta_a A}\left(\frac{\eta_{q,\rm CARMA}}{\eta_{q,\rm NRO45}}\right). \tag{15}$$

Parameters are listed in Table 1.

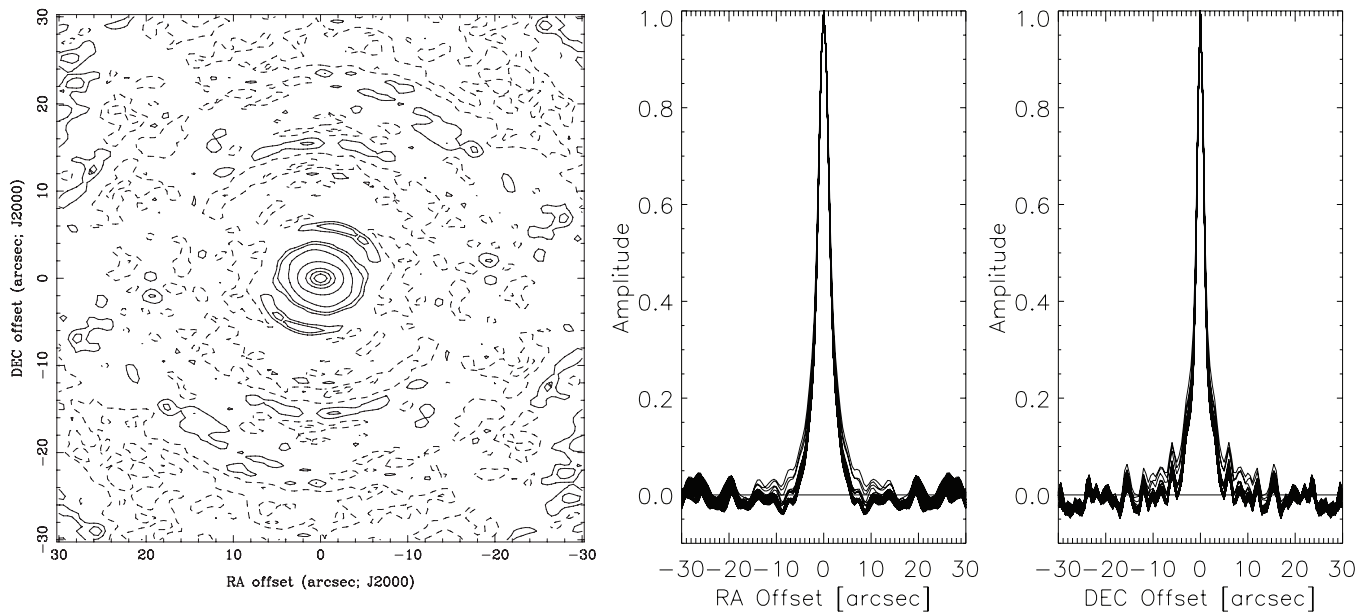

Figure 6. Synthesized beam, i.e., the combination of the four baseline types (CARMA, HATCREEK, OVRO, and NRO45), for robust = +2. Left: synthesized beam pattern. Contours are −4%, −2%, 2%, 4%, 10%, 20%, 40%, 60%, 80%, and 100% of the peak. Dashed lines are negative contours. Middle and right: slices of synthesized beams along R.A. and decl. directions, i.e., a superposition of all the beams at the 151 pointings. The synthesized beam patterns, i.e., uv coverages, are very similar for all the pointings.

5.3. Synthesized Beam Size

The deconvolution process (e.g., CLEAN) replaces a synthesized beam with a convolution beam (typically a Gaussian). We determine the convolution beam size so that its beam solid angle matches that of the synthesized beam. Theoretically, the beam solid angle is an integration of a beam response function over 4π steradians. In principle, we could calculate it by integrating a synthesized beam image or by taking the weight of the zero-spacing data (Appendix B). These methods worked reasonably well, but showed some error, introduced perhaps by the limited size of the beam image (not over 4π steradians). In practice, we found that the following method provides better flux conservation: we calculate the total fluxes of the galaxy with the single-dish map and with the dirty image (with an unknown beam area as a free parameter), and find the beam area that equalizes these total fluxes. The position angle and axis ratio of the beam are derived by a Gaussian fitting to the synthesized beam. The Gaussian is linearly scaled to reproduce the beam area from the flux comparison.

If the solid angles do not match, the total flux is not conserved in the final deconvolved map (e.g., CLEANed map). The CLEANed map has two emission components, deconvolved emission and noise/residual emission, and they have their own units of flux, Jy/(convolution beam) and Jy/(synthesized beam), respectively. Therefore, a convolution beam smaller than the synthesized beam elevates the flux of the residual emission, while a larger beam reduces it. The error becomes particularly problematic for an object with extended, low-flux emission (such as galaxies), which are inherently missed in the deconvolution process, but exist in the CLEANed map. The two units in the final map do not degrade an image quality much in case of the CARMA and NRO45 image, as long as the two beam areas are the same, because the synthesized beam is already similar to a Gaussian beam that we adopt as a convolution beam.

We note that if the deconvolution procedure (such as CLEAN) can "dig" all positive components down to the zero flux level, the convolution beam could have any shape. We also note that in case of pure interferometer observations, the beam solid angle is zero (Appendix B), and thus, this method cannot be applied.

5.4. Joint Imaging and Deconvolution

The procedure for imaging and deconvolution is the same as the one in Section 4.3, but we add the term $W_N I_N$ in Equation (5),

$$I(l, m) = W_H I_H + W_O I_O + W_C I_C + W_N I_N, \qquad (16)$$

where I_N and W_N are the image and weight from the NRO45 visibilities, respectively. W_N is calculated with the pseudo primary beam P_N (Section 5.1) and the theoretical noise σ_N ($=\Delta S^i$) derived with Equation (11).

The number of NRO45 visibilities is a control parameter in this method (Section 5.2), and thus, should not be involved in weighting. Instead, the weight should be calculated solely based on the sensitivity. We use the theoretical noise for weighting. If all visibilities have exactly the same fringe sensitivity, our weighting becomes the same as the conventional "natural" weighting. The sensitivity-based weighting for interferometer data was discussed in Briggs (1995), and our method extends it to the combination with single-dish data.

The robust weighting scheme suppresses the pixels of high natural weights in uv space (Briggs 1995)—if the natural weight is lower than a threshold the weight is unchanged, but if it is higher, the weight of the pixel is set to this threshold. Our weighting scheme reproduces a natural weighting and works with the robust weighting scheme. We made two data cubes with robust = −2 and +2. The resolution of the final combined data cube with robust = −2 is $3''.7 \times 2''.9$ (P.A. = 79°) and 5.08 km s^{-1}. The rms noise is 35 mJy beam^{-1} (i.e., 300 mK) in 10 km s^{-1} channel. robust = +2 gives the resolution of $8''.5 \times 7''.3$ (P.A. = 76°) and 5.08 km s^{-1}, and the rms noise of 52 mJy beam^{-1} (77 mK) in 10 km s^{-1} channel. Figure 6 shows a synthesized beam pattern for robust = +2. Both cubes have the same total luminosity when the synthesized beam sizes are determined as in Section 5.3.

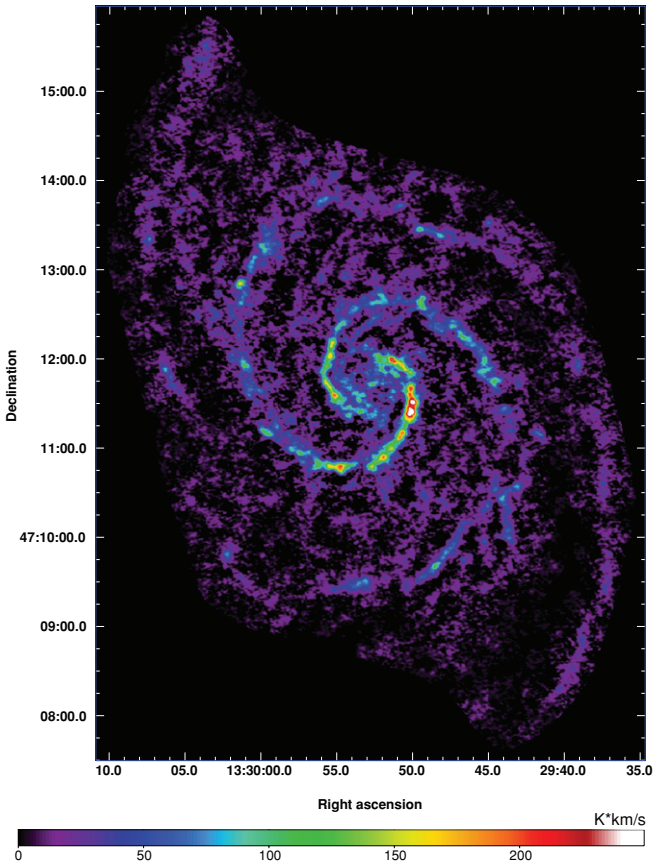

Figure 7. CARMA and NRO45 combined CO ($J = 1$–0) map of M51 with robust $= -2$.

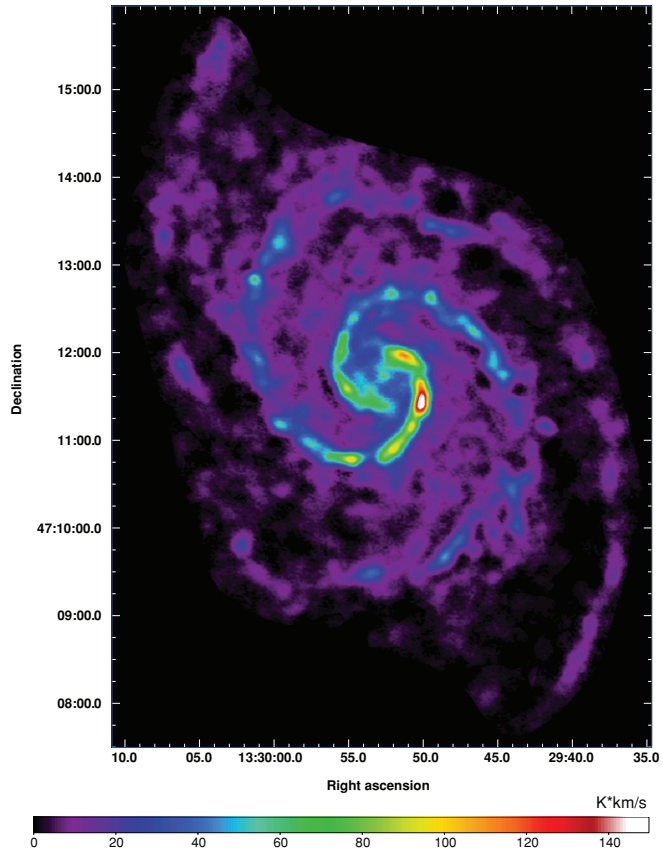

Figure 8. Same as Figure 7, but with robust = +2.

6. INTEGRATED INTENSITY MAP AND IMAGE FIDELITY

Figures 7 and 8 show the CO($J = 1$–0) integrated intensity maps of M51, the combination of CARMA and NRO45 data, with robust= -2 and +2, respectively. These maps are made with the "masked moment method" in Adler et al. (1992). We also dropped the low sensitivity region (outer region) of the CARMA mosaic (see Figure 1). The data with robust $= -2$ is used in following discussions, since it shows finer structures at a higher resolution.

The combination of CARMA (15 antennas) and NRO45 enables a full census of the population of giant molecular clouds (GMCs) over the entire galactic disk. Molecular gas emission in two spiral arms and interarm regions are prominent in this map. Koda et al. (2009) showed the distribution of GMCs both in spiral arms and interarm regions, and the high molecular gas fraction in both regions. These two results suggest that stellar feedback is inefficient to destroy GMCs and molecules, which is supported by a recent analysis by Schinnerer et al. (2010). Molecular structures in the interarm regions were often an issue of debate in previous observations due to poor image fidelity (Rand & Kulkarni 1990; Aalto et al. 1999; Helfer et al. 2003). Figure 9 compares the CO distribution with a *B*-band image from the *Hubble Space Telescope* (*HST*) and an 8 μm image from the *Spitzer Space Telescope*. Dust lanes in the *B*-band image indicate the distribution of the dense interstellar medium, and the 8 μm image shows the distribution of the polycyclic aromatic hydrocarbon (large molecules) illuminated by UV photons from surrounding young stars. The CO emission coincides very well with the dust lanes and 8 μm emission in both spiral arms and interarm regions, which evidences the high image fidelity over a wide range of flux.

Figure 10 shows the NRO45 map (left) and the ratio of the combined map (smoothed to $\sim$20″ resolution) over the NRO45 map, i.e., recovered flux map (right). The recovered flux map shows an almost constant ratio $\sim$1 over the entire map, and no correlation with galactic structures (i.e., no size dependence—in contrast to the dependence expected in pure-interferometer maps). Some extended CO emission is not significantly detected at the high resolution of the combined image, but becomes apparent when the image is smoothed. Note that the companion galaxy NGC 5195 is not included in the CARMA velocity coverage, nor in the combined map, though it is in the NRO45 map.

Both the main galaxy NGC 5194 and companion galaxy NGC 5195 are observed with NRO45. The total flux of NGC 5194 is $(1.022 \pm 0.002) \times 10^4$ Jy km s^{-1} in the NRO45 map, which is consistent with the measurement of Helfer et al. (2003). With the Galactic CO-to-H_2 conversion factor $X_{\rm CO} = 1.8 \times 10^{20}$ cm^{-2}(K km s)$^{-1}$ and the distance of 8.2 Mpc, the total molecular gas mass in NGC 5194 is $4.9 \times 10^9\ M_\odot$. The $X_{\rm CO}$ similar to the Galactic one is found in M51 recently (Schinnerer et al. 2010). The total flux of the combined cube is also 1.0×10^4 Jy km s^{-1}, consistent with the NRO45-only measurement. The total flux and mass of NGC 5195 is 162 ± 4 Jy km s^{-1} and $7.8 \times 10^7\ M_\odot$, respectively. The errors are based on the rms from the map and do not include the systematic error due to the flux calibration in the CARMA observations ($\sim$15%).

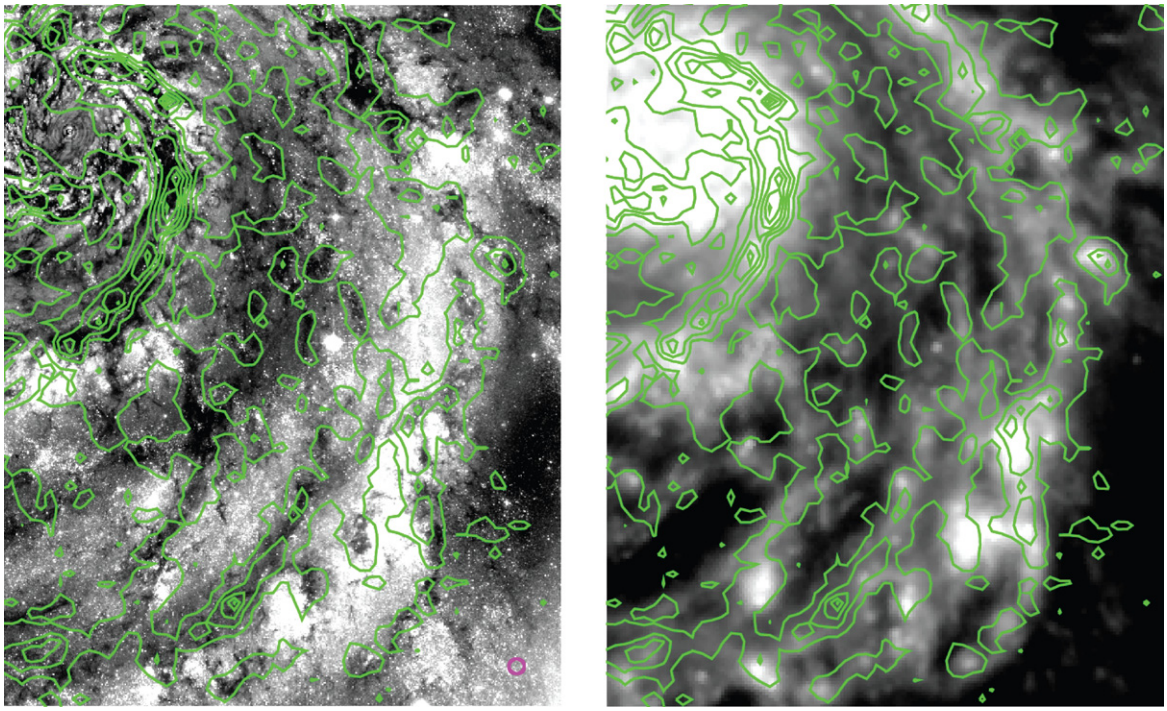

Figure 9. CO contours on an *HST B*-band image (left) and on a *Spitzer* 8 μm image (right). The CO image is first smoothed to a 30″ resolution to mask out $<3\sigma$ pixels in the smoothed image. The CO contours are made with the masked robust $= -2$ map (not with the integrated intensity map), and are the superposition of the 1.5σ, 5.0σ, 10.0σ, and 15.0σ contours in all 10 km s^{-1} channels. The extended emissions at the 1.5σ level are significant in the smoothed image. The *HST* image is derived by dividing the original image by an axisymmetric luminosity profile to visualize the dark dust lanes. The CO emission coincides with the dust lanes both on bright spiral arms and in dimmer interarm regions, indicating the high fidelity of the CO data. The *Spitzer* 8 μm image traces the dense interstellar medium illuminated by UV photons, and the CO coincides with the 8 μm emission as well. The circle at the lower right corner of the left panel has the diameter of 4″ (roughly the size of beam).

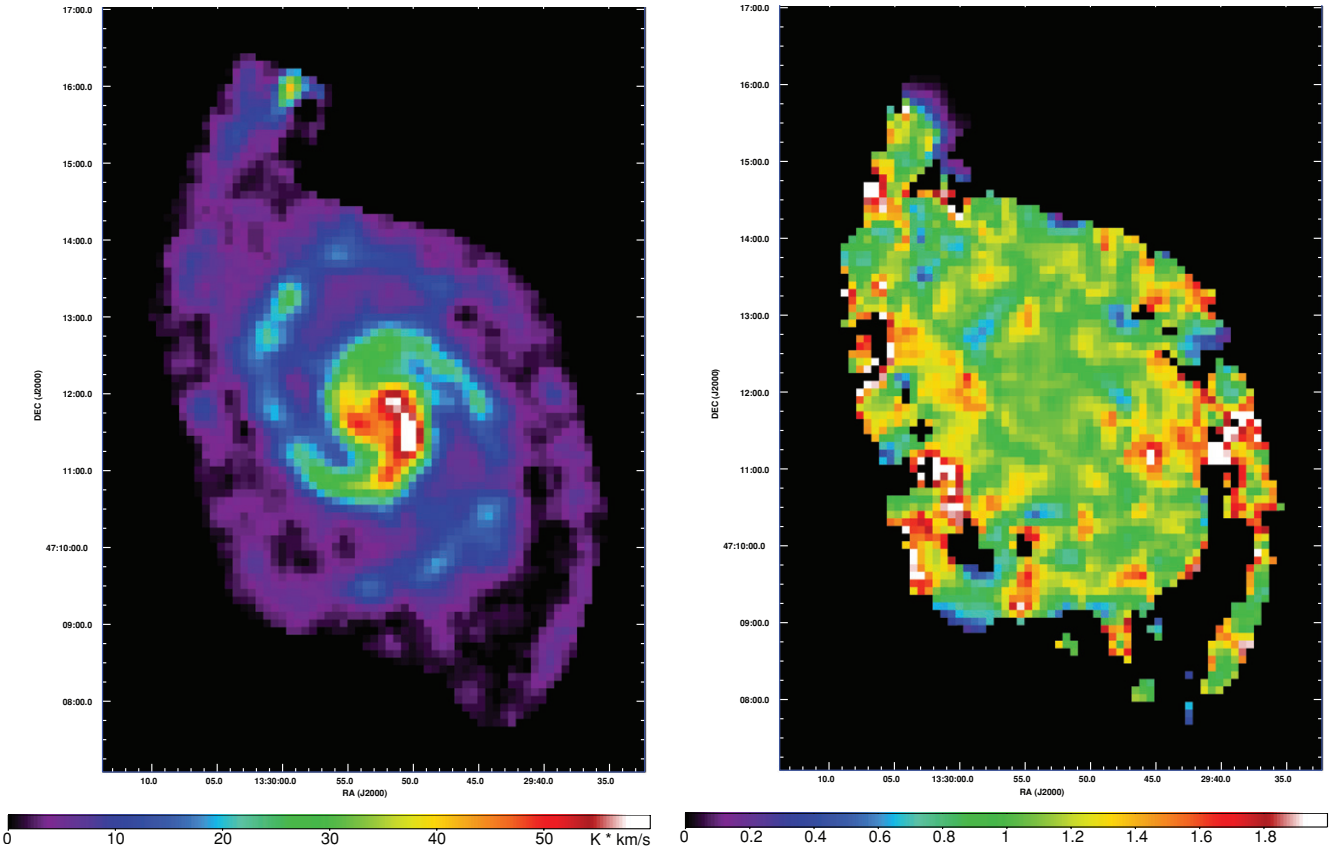

Figure 10. Left: NRO45 CO ($J = 1$–0) map. Right: recovered flux map, i.e., the ratio of the combined map over NRO45 map. The combined map (robust $= -2$) is smoothed to $\sim$20″ resolution for the comparison. The ratio is $\sim$1 over the entire map, and the flux recovery is very good. The companion galaxy NGC 5195 is not in the CARMA velocity coverage. Note that the error in the ratio map varies across the map, depending on the brightness of emission.

7. REQUIREMENTS

There are requirements for sampling, field of view, uv coverage, and sensitivity for single-dish data to be combined with interferometer data in an optimal manner.

First, a spatial fine sampling is necessary (Vogel et al. 1984). The half-beam sampling, a typical practice in most single-dish mapping observations, is not sufficient, since the aliasing effect destroys visibilities *both* at long and very short baselines. Figure 3 illustrates the effect schematically: if the spatial sampling is 10.″3 (= $\lambda_{\rm CO}/52$ m, a typical sampling in NRO45 observations; e.g., Kuno et al. 2007), the tail of the uv distribution leaks into baselines as short as ∼7 m. Hence, the Nyquist sample of 11.″9 (=$\lambda_{\rm CO}/45$ m) is necessary to properly reproduce visibilities up to the 45 m baseline. The observing grid and pixel size in the NRO45 map must be at most 5.″96 (Figure 3).

The single-dish map should cover an area larger than the area of the joint map. The deconvolution with the single-dish beam (Section 5.1.1) causes artifacts at the edges of the images. It is ideal to have extra margins with the width of a few single-dish beam sizes at each image edge.

The sensitivity match between single-dish and interferometer data should also be considered in matching their uv coverages; the maximum effective NRO45 baselines are limited by the matched sensitivity in our observations. Only the baselines of about 1/4–1/3 of the 45 m diameter take practical effect in the combination. It is often discussed that a single-dish telescope needs to be about two times larger than the shortest baseline used in interferometer observations due to uncertainty in the single-dish beam shape and errors in pointing (see Kurono et al. 2009; Corder et al. 2010, and references therein). In our case, the maximum effective baseline is shorter than this length. In practice, interferometer data rarely cover the theoretical minimum baseline (i.e., dish diameter). The long baselines of single-dish data do not have a sensitivity comparable to interferometer's (Section 5.1). To avoid a gap in uv coverage without sensitivity loss, the diameter of the single dish needs to be 3–4 times larger, unless the receiver of the single-dish telescope has a significantly higher sensitivity. The sensitivity match is discussed in detail in Appendix C.

8. COMPARISONS WITH OTHER METHODS

Several methods for the combination of single-dish and interferometer data have been applied at millimeter wavelengths. None of the previous data, however, have a sufficient overlap between single-dish and interferometer uv coverages (in the sense discussed in Section 5.1.1). The weighting schemes are artificial, rather than based on the sensitivity (i.e., data quality). Nevertheless, these methods have some advantages in simplicity as well as disadvantages in detail.

Stanimirovic et al. (1999) introduce a combination method in the image domain. This method is adopted for the BIMA Survey Of Nearby Galaxies (BIMA-SONG) to combine the BIMA interferometer data with the NRAO12 single-dish data (Helfer et al. 2003). They set the weights to be inversely proportional to the beam area (i.e., one term in Equations (9) and (11)) and add the dirty maps and beams of BIMA and NRAO12 linearly (Equation (2)) to produce a joint dirty map and beam. The relative weights are manually and continuously changed with uv distance. The joint dirty map is then CLEANed with the joint synthesized beam. This method starts the combination process from images, rather than visibilities, and is simple. It should be able to use a more natural weighting scheme (e.g., sensitivity uv distribution based on the beam shape and Equation (13); see also Appendix C) if software is developed.

Weiß et al. (2001) also combine a single-dish map and CLEANed interferometer map. They deconvolve the single-dish map with its beam pattern and convolve the result with an interferometer convolution beam, so that the beam attenuation becomes the same for both single-dish and interferometer images. Then, they Fourier transform both images and replace the interferometer data with the single-dish data at the central uv spacing. CLEAN is performed separately for interferometer data alone, which does not take advantage of the high image fidelity of the combined map. Having only one control parameter—the choice of uv range to be replaced—can be advantageous.

Visibilities have been generated from a single-dish map by several authors (Vogel et al. 1984; Takakuwa 2003; Rodríguez-Fernández et al. 2008; Kurono et al. 2009). Our method is in this branch. Helfer et al. (2003) summarize difficulties in setting the weights for this combination scheme and conclude that it is too sensitive to the choice of parameters. Rodríguez-Fernández et al. (2008) and Kurono et al. (2009) suggest setting the relative weight to obtain a cleaner synthesized beam shape, which is advantageous in deconvolution (e.g., CLEAN, MEM). More specifically, Rodríguez-Fernández et al. (2008) set the single-dish weight density in uv space equal to that of the interferometer visibilities that surround the single-dish uv coverage. Kurono et al. (2009) adjusted the relative weight to zero out the total amplitude of the sidelobes of a synthesized beam. Our weighting scheme is more intrinsic to each set of data and is based solely on their qualities; the single-dish weight is independent of the interferometer data and is set based on the rms noise of a single-dish map. The weight is not a parameter of choice.

In pure interferometer imaging, the synthesized beam shape is historically controlled by changing the weight density in uv space. The robust parameter (Briggs 1995) is a famous example that converts the weight smoothly from the natural to uniform weightings. Once the weight is set in our method, the robust weighting works even for the combined data, exactly as designed for pure interferometer data.

9. SUMMARY

We describe the CARMA observations at the early phase of its operation and the OTF observations with the multi-beam receiver BEARS at NRO45. The standard reduction of CARMA and NRO45 data is also discussed and extended to the combined data set case.

We explain the basics of the imaging technique for heterogeneous array data, and show that the combination of interferometer and single-dish data is an extension of the imaging of heterogeneous array data. We introduce a method of combination of interferometer and single-dish data in uv space. The single-dish map is converted to visibilities in uv space. The weights of the single-dish visibilities are determined based on the rms noise of the map, which is more natural than any other artificial weighting schemes. The synthesized beam size is determined to conserve the flux between the dirty beam and the convolution beam. Comparisons with other methods are discussed and the advantages and disadvantages of those methods are summarized. In the Appendices, we discuss the matching of single dish and interferometer sensitivities for the combination of the data.

The resultant map shows the high image fidelity and reveals, for the first time, small structures, such as GMCs, both in bright spiral arms and in faint interarm regions (Koda et al. 2009). From the new map, we calculate that the total masses of NGC 5194 and 5195 are $4.9 \times 10^9\ M_\odot$ and $7.8 \times 10^7\ M_\odot$, respectively, assuming $X_{\rm CO} = 1.8 \times 10^{20}\ {\rm cm}^{-2}\ ({\rm K\,km\,s})^{-1}$.

The combination method is designed on a platform of available software (i.e., MIRIAD) and generates a finite number of discrete visibilities from a single-dish map. Future software should enable data manipulation directly on maps (grids) both in real and Fourier spaces, instead of in visibilities (Appendix D). The weights can be determined on a grid basis, rather than on a visibility basis. Even in such cases, the weights should be determined from the rms noise of the map which are related to the quality of data.

We thank Yasutaka Kurono for insightful comments on an early draft and the anonymous referee for useful comments. We also thank all the CARMA integration team members and the support staff at the Nobeyama Radio Observatory. The Nobeyama 45 m telescope is operated by the Nobeyama Radio Observatory, a branch of the National Astronomical Observatory of Japan. Support for CARMA construction was derived from the Gordon and Betty Moore Foundation, the Kenneth T. and Eileen L. Norris Foundation, the James S. McDonnell Foundation, the Associates of the California Institute of Technology, the University of Chicago, the States of California, Illinois, and Maryland, and the National Science Foundation. Ongoing CARMA development and operations are supported by the National Science Foundation under a cooperative agreement and by the CARMA partner universities. This research was partially supported by HST-AR-11261.01.

Facilities: CARMA, No:45m

APPENDIX A

WEIGHT FUNCTIONS

The dirty image $\bar{I}^{\rm dm}$ and synthesized beam $\bar{B}$ are defined with a set of visibilities $V(u, v)$ as

$$\bar{I}^{\rm dm}(l, m) = \iint V(u, v) W(u, v) e^{2\pi i(ul+vm)} du dv \qquad \text{(A1)}$$

and

$$\bar{B}(l, m) = \iint W(u, v) e^{2\pi i(ul+vm)} du dv, \qquad \text{(A2)}$$

where (u, v) is the coordinates in the uv space.

The sampling and weighting function of visibilities $W(u, v)$ can be written more explicitly as

$$W(u, v) = \sum_{k=1}^{M} R_k T_k D_k \delta(u - u_k, v - v_k), \qquad \text{(A3)}$$

where T_k is the tapering function, and D_k is the density weighting function (see Wrobel & Walker 1999). M is the number of visibilities obtained in observations. T_k and D_k are arbitrary functions, and are often used to control the synthesized beam shape and noise level. For example, the Gaussian taper is $T_k = \exp(-\sqrt{u_k^2 + v_k^2}/2a^2)$ with the half-power beam width $\theta_{\rm HPBW} = \sqrt{2 \ln 2/\pi}/a = 0.37/a$ (rad). The natural and uniform weightings are $D_k = 1$ and $D_k = 1/N_k$, respectively, where N_k is the number of visibilities within a pixel in uv space.

R_k is a weight based on noise, and has the relation $R_k = 1/\Delta S_k^2$ with ΔS_k ($= \Delta S^f$ in Section 4.4.1). The theoretical noise of an image σ can be calculated as

$$\sigma = \sqrt{\left(\sum_{k=1}^{M} T_k^2 D_k^2 R_k\right)\left(\sum_{j=1}^{M} R_j\right)} \Big/ \sum_{i=1}^{M} T_i D_i R_i. \qquad \text{(A4)}$$

APPENDIX B

BEAM SOLID ANGLE

The beam solid angle $\Omega_{\rm A}$ of a synthesized beam (dirty beam) is defined as

$$\Omega_{\rm A} = \iint \bar{B}(l, m) dl dm \qquad \text{(B1)}$$

$$= \iint W(u, v) \left[\iint e^{2\pi i(ul+vm)} dl dm\right] du dv \qquad \text{(B2)}$$

$$= W(0, 0). \qquad \text{(B3)}$$

Equation (A2) is used between Equations (B1) and (B2). The bracket in Equation (B2) is a δ-function. We assumed that the maximum of $\bar{B}(l, m)$ is normalized to 1.

Pure interferometer observations do not have zero-spacing data, and therefore, $\Omega_{\rm A} = 0$. A Gaussian beam $\bar{B}(l, m) = \exp[-(l^2 + m^2)/2\sigma^2]$ has $W(u, v) = 2\pi\sigma^2 \exp[-(u^2 + v^2)/2\sigma_{\rm F}^2]$, where $\sigma_{\rm F} = 1/2\pi\sigma$. Therefore, $\Omega_{\rm A} = 2\pi\sigma^2$.

APPENDIX C

SENSITIVITY MATCHING BETWEEN CARMA AND NRO45

Matching the sensitivities of CARMA and NRO45 is crucial in combination. The sensitivity requirements of the interferometer and single-dish maps are important for the observation plan, and a simple way to calculate matching sensitivities is therefore important.

One approach is to match the sensitivities in uv space around the uv range (baseline range) where two data sets overlap. In other words, we want to match the pixel sensitivities $\Delta S^{\rm p}$ of CARMA and NRO45, i.e., their sensitivities at pixel (u, v). Among some definitions of sensitivity (e.g., Section 4.4.1), the imaging sensitivity $\Delta S^{\rm i}$, i.e., noise fluctuation in the map (Equation (9)), is most used to characterize the quality of map and to estimate the feasibility of observations. Therefore, we first derive the relation between the imaging and pixel sensitivities in uv space.

For simplicity, we assume that all CARMA antennas are identical to each other, having exactly the same $T_{\rm sys}$ and $C_{\rm ij}$. Then, a sensitivity is

$$\Delta S = C_{\rm ij} \frac{T_{\rm sys}}{\sqrt{B \cdot t}}, \qquad \text{(C1)}$$

where B is the channel width and t is the integration time. ΔS is applied to both CARMA and NRO45, and can mean one of the following three sensitivities: fringe sensitivity $\Delta S^{\rm f}$ when t is the integration time of a visibility $t_{\rm vis}$ (Equation (7)); imaging

sensitivity $\Delta S^{\rm i}$ when t is the total integration time, i.e., $t_{\rm vis}N_{\rm vis}$, where $N_{\rm vis}$ is the total number of visibilities; and pixel sensitivity $\Delta S^{\rm p}$ when t is the total integration time of the pixel at (u, v), i.e., $t_{\rm vis}n(u, v)$, where $n(u, v)$ is the number of visibilities in the pixel. Therefore, the imaging and pixel sensitivities are related as

$$\Delta S^{\rm p}(u, v) = \Delta S^{\rm i}\sqrt{\frac{N_{\rm vis}}{n(u, v)}}. \quad \text{(C2)}$$

Hereafter, we derive the relation between $N_{\rm vis}$ and $n(u, v)$.

The $n(u, v)$ for the interferometer (e.g., CARMA) was discussed by Kurono et al. (2009). For a target at a reasonably high declination, synthesis interferometric observations provide a visibility distribution of $n(b) \propto 1/b$, where b is the uv distance $b = \sqrt{u^2 + v^2}$. The visibilities (total of $N_{\rm vis}$) are distributed within the minimum and maximum baseline lengths, $b_{\rm min}$ and $b_{\rm max}$ respectively. From $N_{\rm vis} = \int_{b_{\rm min}}^{b_{\rm max}} n(b)2\pi b db$, we derive

$$n(b) = \frac{N_{\rm vis}}{2\pi(b_{\rm max} - b_{\rm min})}\frac{1}{b}. \quad \text{(C3)}$$

The $n(u, v)$ for a single-dish telescope (e.g., NRO45) is determined by the beam shape of the telescope. We assume a Gaussian beam shape, $\propto \exp[-(l^2+m^2)/2\sigma^2]$, in sky coordinate (l, m). The full width half-maximum (FWHM) of the beam is FWHM $= 2\sqrt{2\ln 2}\sigma$. The $n(u, v)$ is proportional to the Fourier transformation of the beam shape, $\propto \exp[-(2\pi\sigma)^2 b^2/2]$. The total of $N_{\rm vis}$ visibilities are within the uv range from zero to the antenna diameter d. Thus,

$$n(b) = \frac{N_{\rm vis}\cdot 2\pi\sigma^2}{1 - \exp[-(2\pi\sigma)^2 d^2/2]}e^{-\frac{(2\pi\sigma)^2 b^2}{2}}. \quad \text{(C4)}$$

Equation (C2)–(C4) give the pixel sensitivity for interferometer $\Delta S^p_{\rm int}(b)$ and single dish $\Delta S^p_{\rm sd}(b)$. Equalizing these two $\Delta S^p_{\rm int}(b) = \Delta S^p_{\rm sd}(b)$ at $b = b_{\rm overlap}$ where the two uv coverages overlap leads to a relation between the image sensitivities (i.e., rms map noise) of the interferometer and single dish. This relation is a rough measure of the matched sensitivities for the combination of the single-dish and interferometer and would be useful in planning observations. The sensitivity matching can be calculated more accurately with Equation (C2), as performed in Section 5.1.1, if we know an accurate uv coverage $n(u,v)$ of interferometer observations.

Figure 11 plots the pixel sensitivities $\Delta S^{\rm p}$ of CARMA and NRO45 as a function of baseline length b for fixed image sensitivities $\Delta S^{\rm i}$. We set $b_{\rm min}$ and $b_{\rm max}$ to 10 and 300 m (∼4 and 115 kλ), respectively, for CARMA C and D configurations. The CARMA and NRO45 uv coverages overlap significantly between 4 and 10 kλ. The NRO45 noise (sensitivity) increases rapidly beyond the baseline length of about half the diameter (∼8 kλ), and CARMA can complement the uv range beyond that. The imaging sensitivities of our CARMA and NRO45 observations are 27 and 155 mJy in the velocity width of $10\,{\rm km\,s^{-1}}$, respectively. Their sensitivities match around $b \sim$ 4–6 kλ, within the range where the uv coverages overlap.

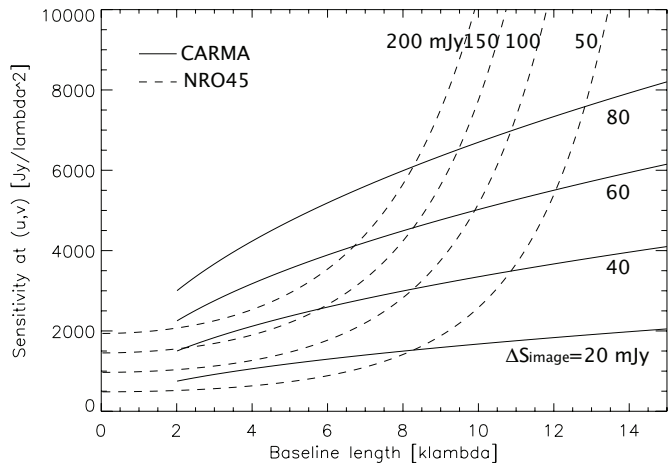

Figure 11. Sensitivity distribution with baseline length for CARMA (solid lines) and NRO45 (dashed lines). The labels are the imaging sensitivities of CARMA and NRO45. The minimum and maximum baseline lengths of CARMA are 10 and 300 m, respectively (for C and D configurations). The sensitivities, pixel sensitivity $\Delta S^{\rm p}$ (y-axis) and imaging sensitivity $\Delta S_{\rm image}(= \Delta S^{\rm i})$, are calculated for the velocity channel width of $\Delta v = 10\,{\rm km\,s^{-1}}$.

APPENDIX D

APPLICATION TO GRID-BASED COMBINATION SCHEME

The new combination technique discussed in this paper converts a single-dish map to a finite number of visibilities (discrete data points in uv space). The weight of each single-dish visibility is determined based on the rms noise of the map (i.e., the quality of the data) using the fringe sensitivity $\Delta S^{\rm f}$ (Equation (13)). In the Fourier transformation, the visibilities are mapped to a grid in uv space, and the pixel sensitivity $\Delta S^{\rm p}$ is calculated for each pixel of the grid by summing up the $\Delta S^{\rm f}$ of all the visibilities in the pixel. The $\Delta S^{\rm p}$ for single-dish data can be calculated directly without going through visibilities once proper software is developed.

The pixel sensitivity $\Delta S^{\rm p}$ for the single-dish data can be defined with Equations (C2) (C4). The rms noise of the single-dish map $\Delta S^{\rm i}$ gives the normalization of the equations. Equation (C4) is for a Gaussian beam, and could be replaced with some other shapes, such as a Fourier transformation of a single-dish beam or PSF if we have better knowledge of them. The $\Delta S^{\rm p}$ for the interferometer data should be calculated from the fringe sensitivities of visibilities $\Delta S^{\rm f}$ using C_{ij} (Equations (7) and (8))—mapping the visibilities onto a grid in uv space and summing up the fringe sensitivities in each pixel. These $\Delta S^{\rm p}$ naturally set the relative weight of the single-dish and interferometer data.

REFERENCES

Aalto, S., Huttemeister, S., Scoville, N. Z., & Thaddeus, P. 1999, ApJ, 522, 165
Adler, D. S., Lo, K. Y., Wright, M. C. H., Rydbeck, G., Plante, R. L., & Alllen, R. J. 1992, ApJ, 392, 497
Briggs, D. 1995, PhD thesis, The New Mexico Institute of Mining and Technology
Corder, S. A., Wright, M. C. H., & Carpenter, J. M. 2010, Proc. SPIE, 7733, 115
Corder, S. A., Wright, M. C. H., & Koda, J. 2010, Proc. SPIE, 7737, 36
Cornwell, T. J. 1988, A&A, 202, 316
Emerson, D. T., & Gräve, R. 1988, A&A, 190, 353
Helfer, T. T., Thornley, M. D., Regan, M. W., Wong, T., Sheth, K., Vogel, S. N., Blitz, L., & Bock, D. C.-J. 2003, ApJS, 145, 259
Koda, J., et al. 2009, ApJ, 700, 32
Kuno, N., et al. 2007, PASJ, 59, 117
Kurono, Y., Morita, K.-I., & Kamazaki, T. 2009, PASJ, 61, 873
Mangum, J. G., Emerson, D. T., & Greisen, E. W. 2007, A&A, 474, 679
Matsushita, S., Kohno, K., Vila-Vilaro, B., Tosaki, T., & Kawabe, R. 1999, Adv. Space Res., 23, 1015
Nakai, N., Kuno, N., Handa, T., & Sofue, Y. 1994, PASJ, 46, 527

Pety, J., & Rodríguez-Fernández, N. 2010, A&A, 517, A12
Rand, R. J., & Kulkarni, S. R. 1990, ApJ, 349, 43
Rodríguez-Fernández, N. J., Pety, J., & Gueth, F. 2008, IRAM Memo 2008-2
Rohlfs, K., & Wilson, T. L. 2000, Tools of Radio Astronomy (Astronomy and Astrophysics Library; New York: Springer)
Sault, R. J., Staveley-Smith, L., & Brouw, W. N. 1996, ApJS, 120, 375
Sault, R. J., Teuben, P. J., & Wright, M. C. H. 1995, in ASP Conf. Ser. 77, Astronomical Data Analysis Software and Systems IV, ed. R. A. Shaw, H. E. Payne, & J. J. E. Hayes (San Francisco, CA: ASP), 433
Sawada, T., et al. 2008, PASJ, 60, 445
Schinnerer, E., Weiß, A., Aalto, S., & Scoville, N. Z. 2010, ApJ, 719, 1588
Sorai, K., Sunada, K., Okumura, S. K., Iwasa, T., Tanaka, A., Natori, K., & Onuki, H. 2000, Proc. SPIE, 4015, 86
Sunada, K., Yamaguchi, C., Nakai, N., Sorai, K., Okumura, S. K., & Ukita, N. 2000, Proc. SPIE, 4015, 237
Stanimirovic, S., Altschuler, D., Goldsmith, P., & Salter, C. 2002, in ASP Conf. Ser. 278, Short-Spacing Correction from the Single-Dish Perspective, ed. S. Stanimirovic et al. (San Francisco, CA: ASP), 375
Stanimirovic, S., Staveley-Smith, L., Dickey, J. M., Sault, R. J., & Snowden, S. L. 1999, MNRAS, 302, 417
Takakuwa, S. 2003, NRO Technical Report, No. 65
Vogel, S. N., Wright, M. C. H., Plambeck, R. L., & Welch, W. J. 1984, ApJ, 283, 655
Weiß, A., Neininger, N., Hüttemeister, S., & Klein, U. 2001, A&A, 365, 587
Wrobel, J. M., & Walker, R. C. 1999, in ASP Conf. Ser. 180, Synthesis Imaging in Radio Astronomy II, ed. G. B. Taylor, C. L. Carilli, & R. A. Perley (San Francisco, CA: ASP), 171